Linear simulations of the cylindrical Richtmyer-Meshkov instability in magnetohydrodynamics

A. Bakhsh, S. Gao, R. Samtaney, and V. Wheatley

Articles you may be interested in

Numerical study of the ablative Richtmyer–Meshkov instability of laser-irradiated deuterium and deuterium-tritium targets
Phys. Plasmas **17**, 112703 (2010); 10.1063/1.3505112

Amplitude reduction of nonuniformities induced by magnetic Rayleigh–Taylor instabilities in Z-pinch dynamic hohlraums
Phys. Plasmas **12**, 012703 (2005); 10.1063/1.1819936

Progress in understanding turbulent mixing induced by Rayleigh–Taylor and Richtmyer–Meshkov instabilities
Phys. Plasmas **10**, 1883 (2003); 10.1063/1.1560923

Laser imprint reduction with a shaping pulse, oscillatory Richtmyer–Meshkov to Rayleigh–Taylor transition and other coherent effects in plastic-foam targets
Phys. Plasmas **10**, 1897 (2003); 10.1063/1.1560616

Rayleigh–Taylor instability: Comparison of hybrid and nonideal magnetohydrodynamic simulations
Phys. Plasmas **5**, 2305 (1998); 10.1063/1.872904
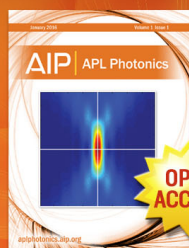
Linear simulations of the cylindrical Richtmyer-Meshkov instability in magnetohydrodynamics

A. Bakhsh,[1] S. Gao,[2,a)] R. Samtaney,[2] and V. Wheatley[3]

[1]*Applied Mathematics and Computational Sciences, CEMSE Division, KAUST, Thuwal, Saudi Arabia*
[2]*Mechanical Engineering, PSE Division, KAUST, Thuwal, Saudi Arabia*
[3]*Mechanical and Mining Engineering, The University of Queensland, Brisbane, Australia*

Numerical simulations and analysis indicate that the Richtmyer-Meshkov instability (RMI) is suppressed in ideal magnetohydrodynamics (MHD) in Cartesian slab geometry. Motivated by the presence of hydrodynamic instabilities in inertial confinement fusion and suppression by means of a magnetic field, we investigate the RMI via linear MHD simulations in cylindrical geometry. The physical setup is that of a Chisnell-type converging shock interacting with a density interface with either axial or azimuthal (2D) perturbations. The linear stability is examined in the context of an initial value problem (with a time-varying base state) wherein the linearized ideal MHD equations are solved with an upwind numerical method. Linear simulations in the absence of a magnetic field indicate that RMI growth rate during the early time period is similar to that observed in Cartesian geometry. However, this RMI phase is short-lived and followed by a Rayleigh-Taylor instability phase with an accompanied exponential increase in the perturbation amplitude. We examine several strengths of the magnetic field (characterized by $\beta = \frac{2P}{B_r^2}$) and observe a significant suppression of the instability for $\beta \leq 4$. The suppression of the instability is attributed to the transport of vorticity away from the interface by Alfvén fronts. © *2016 AIP Publishing LLC.* [http://dx.doi.org/10.1063/1.4943162]

I. INTRODUCTION

The Richtmyer-Meshkov instability (RMI) occurs when a perturbed density interface separating two fluids is subject to an impulsive acceleration, usually by a shock wave.[1,2] The RMI is important in a wide variety of applications. One of the most significant applications is inertial confinement fusion (ICF), which has been a major impetus for the study of shock-accelerated interfaces.[3] In direct-drive ICF, a capsule filled with fuel, typically deuterium and tritium, is placed at the focus of a spherical array of lasers. The lasers heat the surface of the capsule, which drives a converging spherical shock into the target. The goal of this shock compression is to attain sufficiently high temperature and density at the core of the spherical capsule to initiate a fusion reaction. Here RMI becomes a spoiler: it promotes mixing between the capsule material and the fuel. This mixing limits the final compression of the fuel and hence the possibility of achieving energy break-even or production.[4] Lindl *et al.*,[5] in a comprehensive review of the National Ignition Facility at the Lawrence Livermore National Laboratory, state in the final section entitled "The Path Forward" that: "Current evidence points to low-mode asymmetry and hydrodynamic instability as key areas of research to improve the performance of ignition experiments on the NIF and are a central focus of the Ignition Program going forward." It is clear that a key bottleneck towards achieving fusion is hydrodynamic instabilities. The RMI is also important in astrophysical phenomena especially supernovae explosions. It has been used to account for the lack of stratification in the products of supernova 1987A and is now a required component in stellar evolution models.[6] One application

---

a)Present address: Mechanical Engineering, McGill University, Montreal, Quebec H3A 0C3, Canada.

where RMI is beneficial is in supersonic and hypersonic air breathing engines. Here the RMI may be used to enhance the mixing of fuel and air.[7] The RMI also arises in many combustion systems where shock-flame interactions occur; the resulting instability is important in the transition from a deflagration to a detonation.[8]

Nonlinear ideal magnetohydrodynamics (MHD) simulations showed that the RMI could be suppressed in the presence of a magnetic field.[9] The essential mechanism of suppression is the transport of baroclinic vorticity, originally at the interface by the incident shock, by slow- or intermediate-mode shocks, leaving the interface devoid of vorticity and hence suppressing the instability. The suppression was reconfirmed in the context of incompressible MHD linear stability analysis by Wheatley *et al.*,[10] where it was demonstrated that Alfvén fronts were the vehicles of vorticity transport away from the interface. A more detailed investigation followed[11] in which nonlinear MHD simulations demonstrated the RMI suppression and extended the parameter ranges of earlier investigations. In these MHD investigations, the initial seed magnetic field was parallel to the incident shock front. Wheatley *et al.*[12] investigated the case where the magnetic field was parallel to the interface, i.e., there was no normal component of the magnetic field at the interface, and found oscillatory solutions with the RMI still being suppressed. In these prior MHD investigations of RMI, the geometry was planar.

The physical configuration of relevance to ICF is one where the main incident shock is a converging shock. So it is of interest to examine the RM instability in a converging geometry, especially in the presence of a magnetic field, and investigate the physical mechanisms of suppression, if any. One of the early investigations of RMI in cylindrical geometry was carried out by Zhang and Graham,[13] in which they examined both the imploding (shock converging towards cylinder axis) case and the exploding (shock moving radially outwards) case for positive and negative Atwood ratio interfaces. Furthermore, they also examined the growth rate of small amplitude perturbations via "direct numerical simulations" rather than solving the linearized Euler equations. Zhang and Graham write in their paper: "The equations and boundary conditions of the linear theory of RM instability in curved geometry are considerably more complicated than the equations and boundary conditions of the linear theory of RM instability in plane geometry, and to date there is no linear theory for the curved case." It is not uncommon in the RMI literature to encounter linear stability investigations via small amplitude nonlinear simulations. Our approach is different in that we actually solve the linearized equations of motion. Lombardini and Pullin[14] investigated the RMI in cylindrical geometry with azimuthal and axial perturbations in a cylindrical geometry, and developed a linear incompressible theory for the case of an imploding or exploding shock. In particular, they developed a theory for the asymptotic growth rate of perturbations and further derived a unified expression for the asymptotic impulsive growth rate in planar, cylindrical, and spherical cases. An interesting corollary to this analysis was the clear demarcation of effects due to geometry and baroclinic vorticity deposition. The linear analysis was complemented and verified against compressible simulations with a small amplitude perturbation although the simulations were actually performed with a nonlinear code. In converging geometry, the RMI is typically followed by the Rayleigh-Taylor instability (RTI) due to the continued acceleration of the interface towards the center of convergence. This effect was not captured in the model of Lombardini and Pullin.

Linear stability analysis in hydrodynamics has a rich history. Clearly, linear stability analysis of several flows is considered an important precursor to nonlinear stages in the flow development, which in turn is an important stage before turbulence ensues. Indeed, hydrodynamic RM flows follow a similar development: very small amplitude perturbations grow linearly, until they are comparable to the perturbation wavelength, after which nonlinear mode coupling ensues followed by full blown turbulent mixing. It is pointed out there that RMI is not a classical hydrodynamic instability with modal analysis, because the perturbations grow linearly (or linearly in an averaged sense) rather than exponentially. In the original analysis by Richtmyer an initial boundary value problem was derived, where the boundaries were formed by a reflected and a transmitted shock emerging from the zeroth order interaction of an incident shock with a contact discontinuity. The base state in this analysis is a self-similar solution involving a reflected shock, a transmitted shock, and a contact discontinuity that translates at an average constant speed due to the impulse by the incident shock. The linearized compressible inviscid equations were solved by Richtmyer, in which

the perturbation amplitude growth rate undergoes a short transient before settling into an oscillatory state around a constant asymptotic value. Richtmyer himself proposed an impulse model based on an incompressible assumption to obtain the asymptotic growth rate, and this model was in reasonable agreement with the compressible linear solution provided one took into account the post-shock Atwood ratio and the initial compression of the interface by the incident shock. The impulse model itself has been used by a number of researchers to get analytical or semi-analytical models in a number of physical scenarios, and one reason for the widespread use of the impulse model is due to the fact that the initial boundary value problem which must be solved for linear solutions is somewhat complicated. One notable mention in this regard is the work of Mikaelian who investigated the linear RMI and RTI of incompressible flow for a chosen number of spherical concentric shells affected by a radial implosion or explosion.[15] He found analytical solutions for different numbers of spherical shells, ($N = 2, 3$), and presented numerical examples for imploding and exploding shells. He concluded that for $N > 3$, with $N - 1$ interfaces in a system of N fluids, the interface coupling or feedthrough of perturbations from one interface to another will occur. Moreover, he proposed a theoretical model for turbulent mix in spherical geometry. In a follow-on investigation, Mikaelian[16] studied the linear stability of RTI and RMI in cylindrical concentric shells. He performed numerical simulations and illustrated the perturbation from one interface to another of possible gelatin-ring experiments. In addition, he developed a simple model for the evolution of turbulent mix.

Another important development in the linear analysis of RM flows was due to Yang *et al*.[17] who developed their method for the case of a reflected rarefaction wave. Moreover, they provided a solution to the start-up problem for small times. They also examined the validity of the impulse model for the case of the reflected rarefaction. A drawback of both the linear analysis of Richtmyer and Yang *et al*. is that these require specialized numerical methods and codes, and both approaches are somewhat restricted to the case of a single sharp interface. A purely numerical technique to solve the linearized compressible Euler equations in planar geometry, with a time-dependent base state for shock-accelerated density interfaces was proposed by Samtaney.[18] This method is robust enough to be applicable for interfaces that are not sharp, or for paired interfaces forming a layer. This method was extended to linearized compressible MHD in planar geometry and was used in the work of Wheatley *et al*.[10] to compare the analytical growth rate of incompressible MHD with numerical solutions stemming from linearized compressible MHD.

It is evident from an examination of the RMI literature that there is a gap in our knowledge regarding the suppression of RMI in converging geometry in the presence of a magnetic field. Investigations of the MHD RMI thus far have primarily addressed the case where the incident shock propagates from a light gas to a heavy one, corresponding to a positive Atwood number ($A > 0$). Consequently, the effects of cylindrical convergence on the MHD RMI should first be investigated for the $A > 0$ case. Note, however, that the planar MHD RMI is also suppressed for $A < 0$, as clearly illustrated in Fig. 1 of Wheatley *et al*.[11] This is important even in the $A > 0$ case because, although not studied here, the reshock of the interface after shock reflection from the axis of convergence will correspond to a diverging MHD RMI with $A < 0$. It is therefore anticipated that the reshock induced perturbation growth will also be attenuated by the presence of a magnetic field. Clearly, there are a wealth of configurations and parameters for which the cylindrically converging MHD RMI could be investigated. A logical first step in such an investigation is linear stability analysis of an $A > 0$ interface with azimuthal and/or axial perturbations.

The paper is organized as follows: in Section II, the physical setup and the ideal MHD equations are introduced. Here we extend Samtaney's numerical linear stability analysis[18] to MHD in cylindrical geometry. Linearizing the ideal MHD equations about a time dependent base state we derive a set of hyperbolic equations with source terms for the perturbed quantities. These equations are solved using an upwind technique (the details of the numerical method are relegated to the Appendix). In Section III, we present numerical results for both hydrodynamics and MHD for a positive Atwood ratio interface, with purely azimuthal or axial, and combined azimuthal-axial perturbations, accelerated by a Chisnell-type shock.[19] Finally, some conclusions and potential future work are discussed in Section IV.
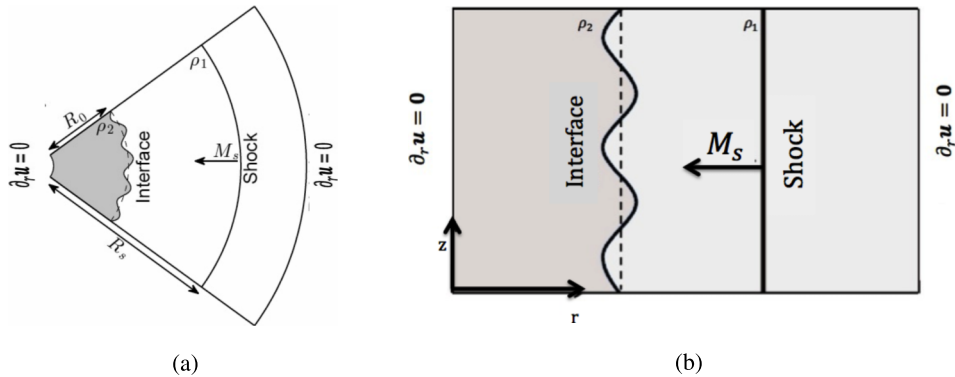
FIG. 1. Schematic diagram of the physical setup: (a) (r, θ)-section with constant z and (b) (r, z)-section with constant θ. Two fluids of densities ρ_1 and ρ_2 are separated by a perturbed interface located at $r = R_0$. A Chisnell-type incident shock is initially located at $r = R_s$, with Mach number M_s.

II. PHYSICAL SETUP AND EQUATIONS

A. Physical setup

A schematic of the physical setup is shown in Fig. 1 (a) for (r, θ)-section with fixed axial coordinate z and (b) for (r, z)-section with constant azimuthal orientation θ. A cylindrical annulus domain is confined by left and right boundaries at $r = R_l$ and $r = R_r$, respectively, with zero gradient boundary conditions. A density interface of azimuthal or axial perturbation wavenumbers m or k is located at $r = R_0$ that separates two fluids of densities ρ_1 and ρ_2. A Chisnell-type converging shock of Mach number M_s travels inwards (further discussion about the Chisnell-type shock in Section III A), which is initialized at $r = R_s$. Samtaney,[9] Wheatley *et al.*,[10] and Wheatley *et al.*[11] studied the suppression of the RMI for the case of an initial magnetic field normal to the plane of the driving incident shock in planar geometry. It was recently made evident by the work of Mostert *et al.*[20] that azimuthal and spherical symmetry may be violated in cylindrical and spherical geometry, respectively, in the presence of a magnetic field. Our intention is to examine the effect of a magnetic field on the RMI in cylindrical geometry in which the base state is only a function of the radial coordinate and employing any of the configurations in Mostert *et al.* would make the base state in our linear stability analysis a multi-dimensional function. To retain simplicity of the base state, our preference is to examine a magnetic field that is initially oriented along the direction of the shock motion so that it results in a purely hydrodynamic incident shock impinging on the density interface. This configuration also implies a somewhat unrealistic radial magnetic field because the solenoidal constraint on the magnetic field precludes a converging purely radial field. Nevertheless, we further justify this choice by trimming the domain of interest and cutting out the origin. At location R_l, the field lines exit the domain radially and do not violate the solenoidal condition outside the domain. A purely radial field inside the domain of interest may be conceivably created by current carrying coils. We do not elaborate on such possibilities because this is beyond the scope of the present study. An additional justification for the choice of a radial field may be made by invoking the benefits of a reductionist approach: our approach is a natural extension of previous studies in planar geometry by including cylindrical geometry effects in a somewhat straightforward manner.

The magnetic field is characterized by its non-dimensional strength using the plasma beta $\beta = 2p/B_r^2$, evaluated at R_0, where p is the initial pressure ahead of the shock and B_r is the radial component of magnetic field strength. Five parameters characterize the problem: the Mach number M_s of the incident Chisnell shock, the Atwood number $A = (\rho_2 - \rho_1)/(\rho_2 + \rho_1)$, the azimuthal or axial perturbation wavenumbers m or k, the plasma β at the interface and the distance ratio R_s/R_0. Our numerical results are completely determined by these five parameters $(M_s, A, m \text{ or } k, \beta, R_s/R_0)$. To limit the scope of our investigation, our simulation domain is chosen to be $R_l = 10^{-5}, R_r = 1.9$, and we fix $M_s = 2.0, A = 0.667$ (this Atwood ratio corresponds to, for example, an air-SF$_6$ interface

which is a common combination used in several previous RMI investigations) and $R_s/R_0 = 1.2/1.0$ and mainly study the cases of different perturbation wavenumbers m or k, and plasma β.

B. Governing equations

The time-scale for diffusion is much longer than the convective time scale in RMI. Hence we neglect viscous, thermal, and plasma resistivity effects. Hence, the governing equations are those of ideal MHD written below in conservation form in cylindrical coordinates:

$$\frac{\partial U}{\partial t} + \frac{1}{r}\frac{\partial(rF(U))}{\partial r} + \frac{1}{r}\frac{\partial G(U)}{\partial \theta} + \frac{\partial H(U)}{\partial z} = S, \tag{1}$$

where $U \equiv U(r,\theta,z,t) = \{\rho, \rho u_r, \rho u_\theta, \rho u_z, B_r, B_\theta, B_z, e\}^T$ is the solution vector, ρ is the density, $(\rho u_r, \rho u_\theta, \rho u_z)$ is the momentum, (B_r, B_θ, B_z) is the magnetic field, e is the total energy per unit volume. These equations are already expressed in non-dimensional form by choosing a reference density, pressure, and length scale (for example, see Wheatley *et al.*[12] for the non-dimensionalization). $F(U)$, $G(U)$, and $H(U)$ are the fluxes of mass, momentum, magnetic flux, and energy in the r, θ, and z directions given as

$$F = \begin{bmatrix} \rho u_r \\ \rho u_r^2 + \tilde{p} - B_r^2 \\ \rho u_r u_\theta - B_r B_\theta \\ \rho u_r u_z - B_r B_z \\ 0 \\ u_r B_\theta - u_\theta B_r \\ u_r B_z - u_z B_r \\ (e + \tilde{p})u_r - (\mathbf{B} \cdot \mathbf{u})B_r \end{bmatrix}, G = \begin{bmatrix} \rho u_\theta \\ \rho u_r u_\theta - B_r B_\theta \\ \rho u_\theta^2 + \tilde{p} - B_\theta^2 \\ \rho u_\theta u_z - B_\theta B_z \\ u_\theta B_r - u_r B_\theta \\ 0 \\ u_\theta B_z - u_z B_\theta \\ (e + \tilde{p})u_\theta - (\mathbf{B} \cdot \mathbf{u})B_\theta \end{bmatrix},$$

$$H = \begin{bmatrix} \rho u_z \\ \rho u_r u_z - B_r B_z \\ \rho u_\theta u_z - B_\theta B_z \\ \rho u_z^2 + \tilde{p} - B_z^2 \\ u_z B_r - u_r B_z \\ u_z B_\theta - u_\theta B_z \\ 0 \\ (e + \tilde{p})u_z - (\mathbf{B} \cdot \mathbf{u})B_z \end{bmatrix}, \tag{2}$$

where $\tilde{p} = p + \frac{1}{2}(\mathbf{B} \cdot \mathbf{B})$ is the sum of gas and the magnetic pressures. S is a source term arising in cylindrical coordinates, given by

$$S = -\frac{1}{r}\left[0, B_\theta^2 - \rho u_\theta^2 - \tilde{p}, \rho u_r u_\theta - B_r B_\theta, 0, 0, u_\theta B_r - u_r B_\theta, 0, 0\right]^T. \tag{3}$$

To close the system we use the perfect gas equation of state so that $e = \frac{p}{\gamma - 1} + \frac{1}{2}(\mathbf{B} \cdot \mathbf{B}) + \frac{1}{2}\rho(\mathbf{u} \cdot \mathbf{u})$, where γ is the ratio of specific heats fixed at $5/3$. Finally, we have the solenoidal constraint on the magnetic field, i.e., $\nabla \cdot \mathbf{B} = 0$.

The initial magnetic field has an inverse radial dependence. Close to the origin, large numerical errors are encountered owing to a lack of analytical cancellation of a term proportional to r^{-3} in the radial momentum equation. These errors are eliminated by rewriting the radial component of the magnetic field as $B_r = B_r^* + B_r^1$ where $B_r^* = \frac{\beta}{r}$ is a curl-free portion of the magnetic field. The ideal MHD equations are rewritten as

$$\frac{\partial \tilde{U}}{\partial t} + \frac{1}{r}\frac{\partial(r\tilde{F}(\tilde{U}))}{\partial r} + \frac{1}{r}\frac{\partial \tilde{G}(\tilde{U})}{\partial \theta} + \frac{\partial \tilde{H}(\tilde{U})}{\partial z} = \tilde{S}, \tag{4}$$

where $\tilde{U} = \{\rho, \rho u_r, \rho u_\theta, \rho u_z, B_r^1, B_\theta, B_z, \tilde{e}\}^T$. Also, the modified fluxes and source terms are

$$\tilde{F} = \{\rho u_r, \rho u_r^2 + \tilde{p}_t - B_r B_r^1, \rho u_r u_\theta - B_r B_\theta, \rho u_r u_z - B_r B_z, 0, u_r B_\theta - u_\theta B_r, u_r B_z$$
$$- u_z B_r, (\tilde{e} + \tilde{p}_t + B_r^* B_r^1) u_r - (\mathbf{B.u}) B_r\}^T, \tag{5}$$

$$\tilde{G} = \{\rho u_\theta, \rho u_r u_\theta - B_r B_\theta, \rho u_\theta^2 + \tilde{p}_t - B_\theta^2, \rho u_\theta u_z - B_\theta B_z, u_\theta B_r - u_r B_\theta, 0, u_\theta B_z$$
$$- u_z B_\theta, (\tilde{e} + \tilde{p}_t + B_r^* B_r^1) u_\theta - (\mathbf{B.u}) B_\theta\}^T, \tag{6}$$

$$\tilde{H} = \{\rho u_z, \rho u_r u_z - B_r B, \rho u_\theta u_z - B_\theta B_z, \rho u_z^2 + \tilde{p}_t - B_z^2, u_z B_r - u_r B_z, u_z B_\theta$$
$$- u_\theta B_z, 0, (\tilde{e} + \tilde{p}_t + B_r^* B_r^1) u_z - (\mathbf{B.u}) B_z\}^T, \tag{7}$$

$$\tilde{S} = -\frac{1}{r} \{0, B_\theta^2 - \rho u_\theta^2 - \tilde{p}_t + B_r^* B_r^1, \rho u_r u_\theta - B_r B_\theta, 0, 0, u_\theta B_r - u_r B_\theta, 0, , 0\}^T, \tag{8}$$

where $\tilde{e} = \frac{p}{\gamma-1} + \frac{1}{2}((B_r^1)^2 + B_\theta^2 + B_z^2) + \frac{1}{2}\rho(u_r^2 + u_\theta^2 + u_z^2)$ and $\tilde{p}_t = p + \frac{1}{2}((B_r^1)^2 + B_\theta^2 + B_z^2)$.

To examine the linear stability of a converging shock interacting with a perturbed interface, we linearize the ideal MHD equations by splitting the solution into a base and perturbed solutions as $\tilde{U}(r, \theta, z, t) = \mathring{U}(r, t) + \epsilon \hat{U}(r, t) e^{i(m\theta + kz)}$, where m and k denote the azimuthal and axial perturbation wavenumbers and $i \equiv \sqrt{-1}$. The time dependent base state is a function of the radial coordinate, and comprises of shocks and a contact discontinuity. Details of the base state are presented later. Substituting the base and perturbed solutions into the governing equations, we get the partial differential equations governing the base and perturbed states as follows:

$$\frac{\partial \mathring{U}}{\partial t} + \frac{1}{r} \frac{\partial}{\partial r} (r F(\mathring{U})) = \mathring{S}, \tag{9a}$$

$$\frac{\partial \hat{U}}{\partial t} + \frac{1}{r} \frac{\partial}{\partial r} (r M(\mathring{U}) \hat{U}) + \frac{1}{r} i m N(\mathring{U}) \hat{U} + i k P(\mathring{U}) \hat{U} = \hat{S}, \tag{9b}$$

$$\mathring{S} = \begin{bmatrix} 0 \\ -\frac{1}{r}[\mathring{B}_\theta^2 - \mathring{\rho}\mathring{u}_\theta^2 - \mathring{p}_t + B_r^*\mathring{B}_r^1] \\ -\frac{1}{r}[\mathring{\rho}\mathring{u}_r\mathring{u}_\theta - \mathring{B}_r\mathring{B}_\theta] \\ 0 \\ 0 \\ -\frac{1}{r}[\mathring{u}_\theta\mathring{B}_r - \mathring{u}_r\mathring{B}_\theta] \\ 0 \\ 0 \end{bmatrix}, \hat{S} = \begin{bmatrix} 0 \\ -\frac{1}{r}[2\mathring{B}_\theta\hat{B}_\theta - 2\mathring{\rho}\mathring{u}_\theta\hat{u}_\theta - \mathring{\rho}\hat{u}_\theta^2 - \hat{p}_t + B_r^*\hat{B}_r^1] \\ -\frac{1}{r}[\mathring{\rho}\mathring{u}_r\hat{u}_\theta + \mathring{\rho}\hat{u}_r\mathring{u}_\theta + \mathring{\rho}\hat{u}_r\mathring{u}_\theta - \mathring{B}_r\hat{B}_\theta - \hat{B}_r\mathring{B}_\theta] \\ 0 \\ 0 \\ -\frac{1}{r}[\hat{u}_\theta\mathring{B}_r + \mathring{u}_\theta\hat{B}_r - \hat{u}_r\mathring{B}_\theta - \mathring{u}_r\hat{B}_\theta] \\ 0 \\ 0 \end{bmatrix}, \tag{10}$$

where $M(\mathring{U})$, $N(\mathring{U})$, and $P(\mathring{U})$ are, respectively, the Jacobians of the fluxes $\tilde{F}, \tilde{G}$, and $\tilde{H}$ with respect to the base state. We note here that Eqs. (9a)–(10), derived from ideal MHD equations, are scale-free and as such one may choose the radial domain extent arbitrarily.

Equations (9a) and (9b), governing the base and perturbed state, respectively, are both hyperbolic partial differential equations. These are numerically solved with an explicit time marching upwind procedure. The details of the numerical method are given in the Appendix.

III. LINEAR STABILITY RESULTS

In this section, we present results from linear stability simulations. We begin by examining the time dependent radially varying base state solution, followed by the perturbed quantities for hydrodynamics and MHD: both of these are presented first for purely azimuthal perturbations

($m \neq 0, k = 0$), for purely axial perturbations ($m = 0, k \neq 0$), and combined axial-azimuthal perturbations ($m \neq 0, k \neq 0$). In particular, we focus on vorticity in the domain as we consider the baroclinic vorticity to be the dominant mechanism driving the instability of the interface. We also present comparisons with nonlinear simulations. In all cases, except when specified otherwise, the radial domain is discretized with 1600 cells. As briefly shown for a specific case in Section III E, differences in growth rates between employing 1600 or 8000 cells are small.

A. Base state solution

The time-dependent base state equations are independent of perturbed state variables; the azimuthal, m, and axial perturbation, k wavenumbers. Besides, choosing $\mathring{B}_r$ to be inversely proportional to radius, the induction equation is satisfied identically and decoupled from the other equations.

The base state is examined by plotting the density profiles at time $t = 0.0$ (initial condition) and $t = 0.552$ in Fig. 2. At $t = 0$, the r-dependent flow field behind the initialized circularly converging gas-dynamic shock is computed based on the approximate analysis by Chisnell[19] and is dubbed the "Chisnell-type" shock. Chisnell's analysis provides the radial variation of the density, radial velocity, and pressure behind the shock as a function of radius. It turns out that at $t = 0$ the density profile is a mildly increasing function of radius just behind the shock (see Fig. 2), whereas the radial velocity and pressure decrease in magnitude behind the shock front (not shown). Specifying a constant state behind the shock, while convenient, leads to disturbances which are best avoided. An alternative to this so-called Chisnell-type shock would be to employ a circular Riemann problem to drive a shock onto the interface. Although this latter method is also convenient, it results in extra waves, i.e., a contact and rarefaction wave, in addition to a shock. The reflected waves from the shock-density interface may subsequently interact with the contact and can be re-reflected and affect the results of the linear analysis. Hence the circular Riemann problem is not our choice to induce the incident shock. The Chisnell-type incident shock (labeled "IS") is perhaps the cleanest technique for generating a single radially moving shock. IS moves radially towards the contact discontinuity (labeled as "CD") and refracts into a transmitted shock and a reflected shock (labeled as "TS" and "RS").

The density spacetime diagram illustrates the wave diagram of the base state more clearly. The density interface (CD) is a vertical line in Fig. 3 indicating that it is stationary until it interacts with the incident Chisnell-type shock (IS). Then, the IS bifurcates into a transmitted shock (TS) and a reflected shock (RS). The IS provides an impulse to the CD accelerating it which is seen between the two shocks RS and TS. Although the CD appears to be a straight line in the spacetime diagram, the second time derivative is in fact non-zero. We note that at $t = 0.552$, the transmitted shock is about to leave the domain and therefore, all the results are generated until this time. In Fig. 4 the base velocity $\mathring{u}_r$ of the CD is plotted, where it shows that as the CD approaches the origin it decelerates. As discussed later, this deceleration (or negative acceleration) is responsible for a Rayleigh-Taylor (RT) phase of the instability of the interface. Hence, the interface is subject
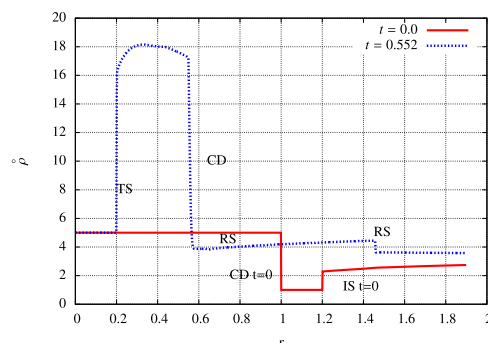

FIG. 2. Density profiles of base state at $t = 0.0$ (initial conditions) and $t = 0.552$. IS denotes the incident shock, TS denotes the transmitted shock, RS denotes the reflected shock, and CD is the contact discontinuity.
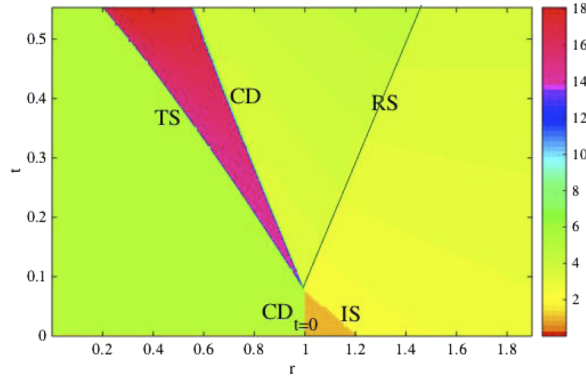
FIG. 3. Spacetime diagram of density field of the base state. IS denotes the incident shock, TS denotes the transmitted shock, RS denotes the reflected shock, and CD is the contact discontinuity.

to an impulsive acceleration by the IS (resulting in the RMI) and a continuous acceleration phase due to geometric effects (resulting in the RTI). Fig. 5(a) shows the impulsive acceleration of the interface by the interaction with the incident shock; while the magnified portion in Fig. 5(b) is the acceleration of the interface as it moves towards the origin. We demarcate the RMI from the RTI phase at $t \approx 0.21$ in our simulations.

B. Evolution of the perturbations

In this section, the results for hydrodynamics (HD) (i.e., $\beta = \infty$), and MHD (i.e., finite β) are presented. Following Lombardini and Pullin[14] we non-dimensionalize the time scale using $1/(a_0 K)$ as our reference time scale, where a_0 is the unshocked sound speed ahead of the incident shock, $K = m/R_0(k)$ for purely azimuthal (axial) modes. The perturbation growth rate $\dot{h}$ is normalized by the theoretical growth rate $\dot{h}_\infty$ expressed as

$$\dot{h}_\infty = \frac{F_{M_s} h_0^+ \Delta W (1 + K A^+)}{R_0},\tag{11}$$

where ΔW is the impulsive change in the interface velocity, A^+ is the post-shock Atwood number, F_{M_s} is a parameter depending on Mach number of the incident shock ($F_{M_s} = 0.85$ for our cases).[14] h_0^+ the initial perturbation amplitude, which in linear stability cancels out, is chosen as unity for convenience.

1. Solution details for hydrodynamics

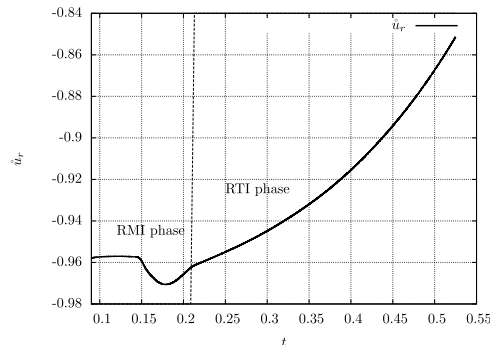We begin our discussion with the hydrodynamics case followed by MHD results.

FIG. 4. Time history of radial velocity $\mathring{u}_r$ at CD.
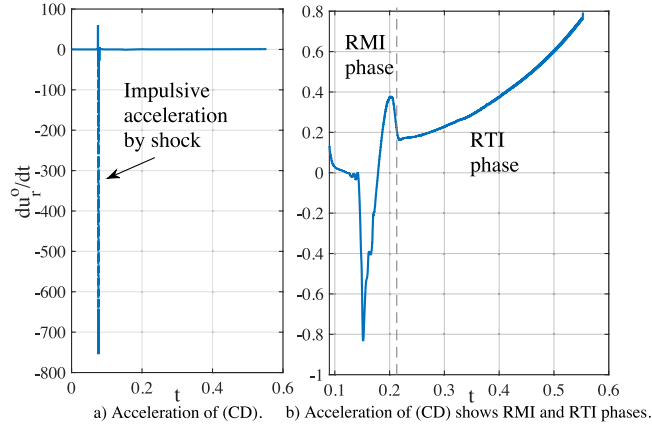
FIG. 5. Time history of (a) acceleration of CD, (b) acceleration of CD with approximate demarcation of RMI and RTI phases.

a. Purely azimuthal perturbations. We now examine the case of purely azimuthal perturbations, in which there is no variation of the solution in the z direction. The scaled growth rate history is plotted in Fig. 6 for different perturbation wavenumbers $m = 16, 64, 128, 256$. The growth rate for the largest wave number case $m = 256$ in hydrodynamics is similar to the Cartesian geometry case until about scaled time $a_0 t m / R_0 \approx 30$. The growth rate increases from zero and then oscillates around unity; this is the asymptotic growth rate one would attain in Cartesian geometry. However, in our cylindrical case, as the interface approaches the origin, the RTI manifests itself and we observe an exponential increase in magnitude of the growth rate. The onset of RTI and its distinction from the RMI phase is most evident for the largest wavenumber ($m = 256$), while the distinct separation between RMI and RTI for smaller wavenumber is not very clear and for the lowest perturbation wave number ($m = 16$) the RTI lasts only a short time. In all cases, the exponential growth during the RTI results in a phase reversal of the amplitude. The spatial variation of the perturbed radial and azimuthal components of the velocity, perturbed pressure, and z-component of the vorticity are plotted in Fig. 7 at $t = 0.552$. The radial velocity component shows a large negative peak at the interface location (the average position of the interface in the base state solution is superimposed on the perturbed radial velocity). This magnitude of this peak corresponds to the growth rate of the interface amplitude. During the refraction of the incident shock at the interface, vorticity is deposited because of the baroclinic source term, and is the essential driving mechanism of the RMI, as discussed by Hawley and Zabusky[21] and Samtaney and Zabusky.[22] The z-component of the vorticity $\hat{\omega}_z = \frac{1}{r} \frac{\partial (r \hat{u}_\theta)}{\partial r} - \frac{1}{r} i m \hat{u}_r$ is a vortex sheet (VS) for a sharp interface and visible as a large peak in Fig. 7(d). In this case with zero magnetic field, the position of the VS coincides with the position of the interface. This can also be seen as the large gradient in $\hat{u}_\theta$ at the interface in Fig. 7(b).

After the primary interaction of the shock at the interface, secondary waves propagate along the azimuthal direction. These secondary interactions are manifested in our linear simulations as the
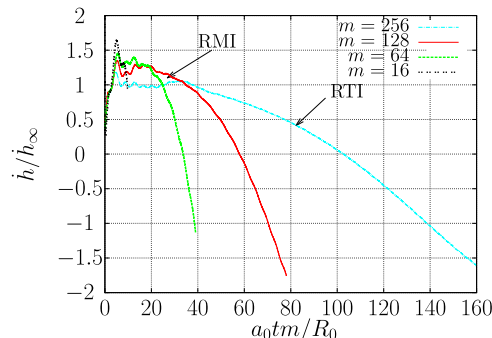

FIG. 6. Time history of scaled growth rate in hydrodynamics for azimuthal perturbation wavenumber $m = 16, 64, 128, 256$.
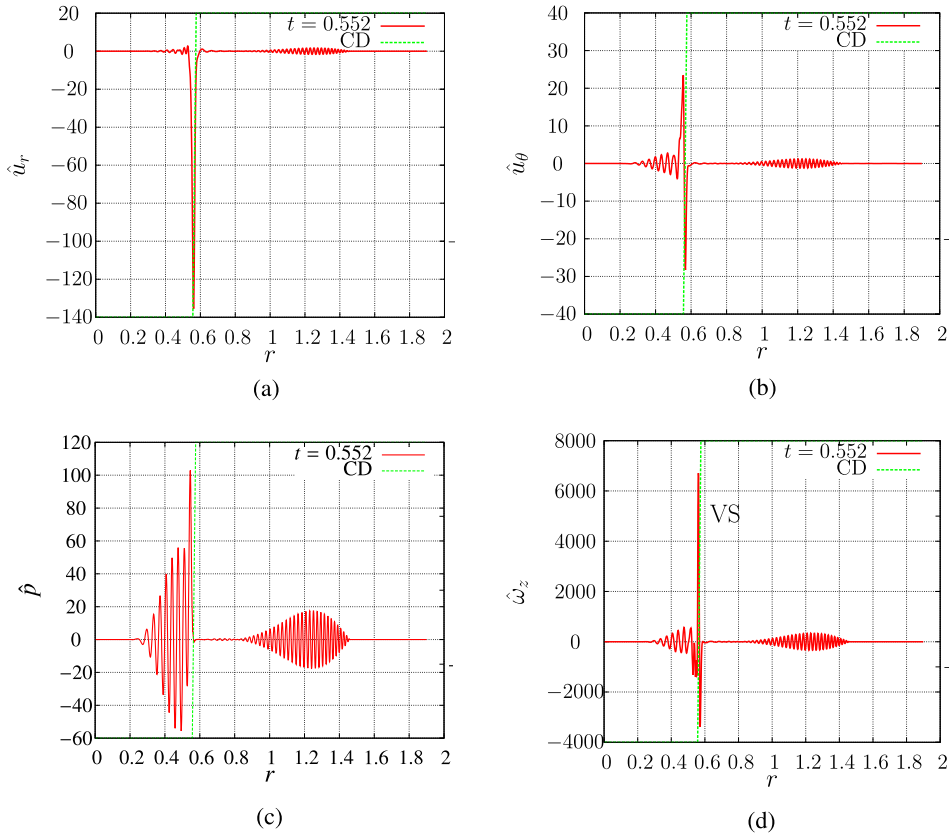
FIG. 7. Profiles of perturbed variables in hydrodynamics at $t = 0.552$: (a) r-component of velocity, (b) θ-component of velocity, (c) pressure, (d) z-component of vorticity. The azimuthal perturbation wavenumber is $m = 256$.

oscillations of the fields between the interface and the reflected/transmitted shocks. The wavelength of these oscillations decreases with increasing azimuthal wavenumber m. The secondary interactions also leave a signature on the growth rate in the form of oscillations before the RTI overwhelms the RMI growth rate (see Fig. 6).

    b. Purely axial perturbations. We plot the scaled growth rate history for different perturbation wavenumbers $k = 16, 64, 128, 256$ in Fig. 8. Similar to the case of purely azimuthal perturbations, the growth rate for purely axial perturbations exhibits an initial rapid increase, after which the perturbation growth rate oscillates around a constant value for a short duration followed by the exponential increase in the magnitude of the growth rate because of the RTI. The onset of RTI is clear for the largest wavenumber ($k = 256$), although for a smaller one ($k = 16$), the demarcation
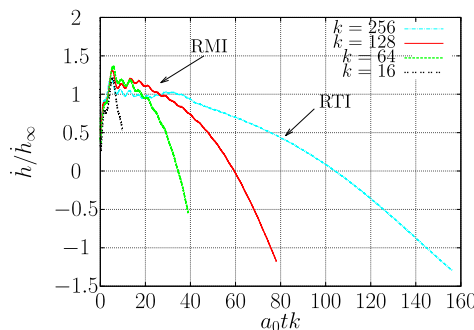

FIG. 8. Time history of scaled growth rate in hydrodynamics for axial perturbation wavenumber $k = 16, 64, 128, 256$.
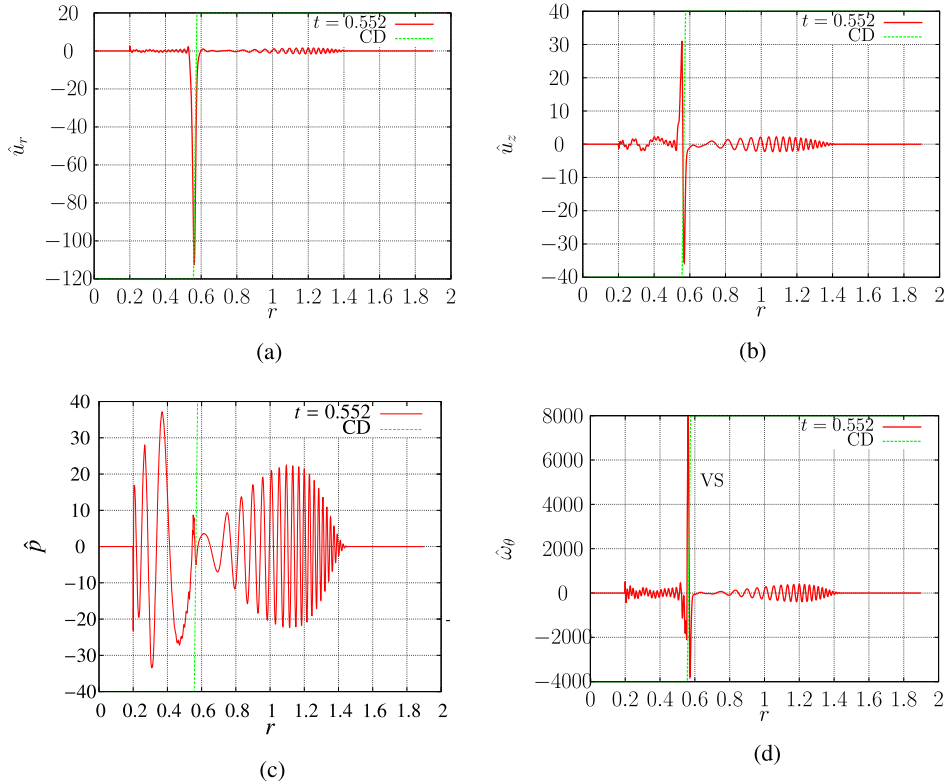
FIG. 9. Profiles of perturbed variables in hydrodynamics at $t = 0.552$: (a) r-component of velocity, (b) z-component of velocity, (c) pressure, (d) θ-component of vorticity. The axial perturbation wavenumber is $k = 256$.

between RMI and RTI is not so apparent. For the highest axial wave number ($k = 256$) the perturbed radial and azimuthal components of the velocity, perturbed pressure, and θ-component of the vorticity $\hat{\omega}_\theta = ik\hat{u}_r - \frac{\partial \hat{u}_z}{\partial r}$ are plotted in Fig. 9 at $t = 0.552$. The behavior of these fields is very similar to those observed for the azimuthal case. The peak vorticity magnitude is coincident with the mean interface position and the peak magnitude of the radial velocity (also on the interface) corresponds to the growth rate of the perturbation amplitude. The secondary waves are manifested as oscillations between the interface and the reflected/transmitted shocks.

    c. Combined azimuthal-axial perturbations. We now examine a combination of three dimensional azimuthal and axial perturbations. Following Ref. 14, the time scale is non-dimensionalized by $R_0/(a_0K)$, where the combination of two wavenumbers $K = \sqrt{(m^2 + k^2 R_0^2)}$ is used in 3D modes. The growth rate is non-dimensionalized by the same factor given in Equation (11).

    The time histories of normalized growth rate in the hydrodynamics case for different combinations of axial/azimuthal wavenumbers $(k, m) = (16, 16), (64, 64), (128, 128), (256, 256)$ are plotted in Fig. 10. The overall behavior of growth rate is similar to that seen for purely axial and azimuthal wave numbers. One interesting feature is that after the onset of RTI, the same total axial/azimuthal combination with the larger azimuthal contribution has a larger growth of the RTI. This is also evident by comparing the purely axial (k = 256) and azimuthal perturbations (m = 256) in Figures 6 and 9: the growth rate is larger during RTI for the azimuthal case than the corresponding axial one with the same wave number.

2. Solution details of MHD

    Several values of β characterizing the strength of the magnetic field are examined. Here we present the details of the solution for $\beta = 4$ for purely azimuthal and purely axial perturbations. A discussion of varying β will be presented later in Section III E.
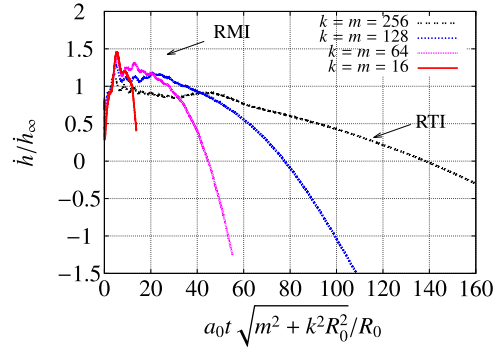
FIG. 10. Time history of scaled growth rate in HD for 3D perturbation wave numbers $k = m = 16, 64, 128, 256$.

a. Purely azimuthal perturbations. In Fig. 11, we plot the time history of scaled growth rate in MHD for different perturbation wavenumbers $m = 16, 64, 128, 256$. For the two largest wavenumber case ($m = 256, 128$), the growth rate increases initially and then reduces because of the magnetic field. During the time duration of the linear simulation, the growth rate eventually reduces and oscillates around a small value below zero. Recall that in Cartesian geometry, the growth rate at the interface is suppressed by the magnetic field and it oscillates around the asymptotic value zero (see Ref. 18 for examples). We conjecture that, at the late time stage for these cases, vorticity is being continually generated at the accelerating interface, and MHD waves remove it continuously from the interface. This probably results in a small residual growth rate. For the smaller wavenumber cases ($m = 64, 16$), the time duration of the simulation is insufficient for any large suppression to occur. In all these cases, the onset of RTI is not clearly demarcated from the RMI phase.

Because the suppression is largest for the highest wavenumber, as one may intuitively expect, we now examine the solution details and elucidate the suppression mechanisms for $m = 256$. The perturbed r- and θ-components of velocity, r- and θ-components of magnetic field, z-component of vorticity, and z-component of current density $\hat{j}_z$ (defined as $\hat{j}_z = \frac{1}{r}\frac{\partial(r\hat{B}_\theta)}{\partial r} - \frac{1}{r}im\hat{B}_r$) are plotted in Fig. 12. Wheatley *et al.*,[10] in analysis of impulsively accelerated interfaces in the context of incompressible MHD, concluded that Alfvén fronts transport vorticity away from the interface and constitute the main mechanism for the RMI suppression. A similar behavior is observed in our linear simulations. Fig. 12(e) shows two dominant vortex sheets which coincide with Alfvén fronts evident in the current density in Fig. 12(f). As in the planar case, these Alfvén fronts transport vorticity away from the interface and hence stabilize the interface.

b. Purely axial perturbations. The time history of scaled growth rate in MHD is plotted in Fig. 13, for different perturbation wavenumbers $k = 16, 64, 128, 256$. For the two largest wavenumber case ($k = 256, 128$), the growth rate increases initially followed by a reduction because of the magnetic field. During the time duration of the investigation, the growth rate eventually reduces and
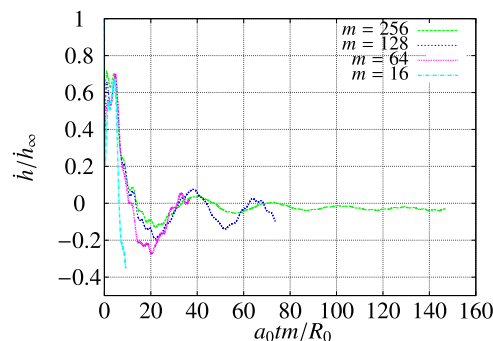

FIG. 11. Time history of scaled growth rate in MHD for azimuthal perturbation wavenumbers $m = 16, 64, 128, 256$. The initial plasma beta is $\beta = 4$ at the interface $R_0 = 1.0$.
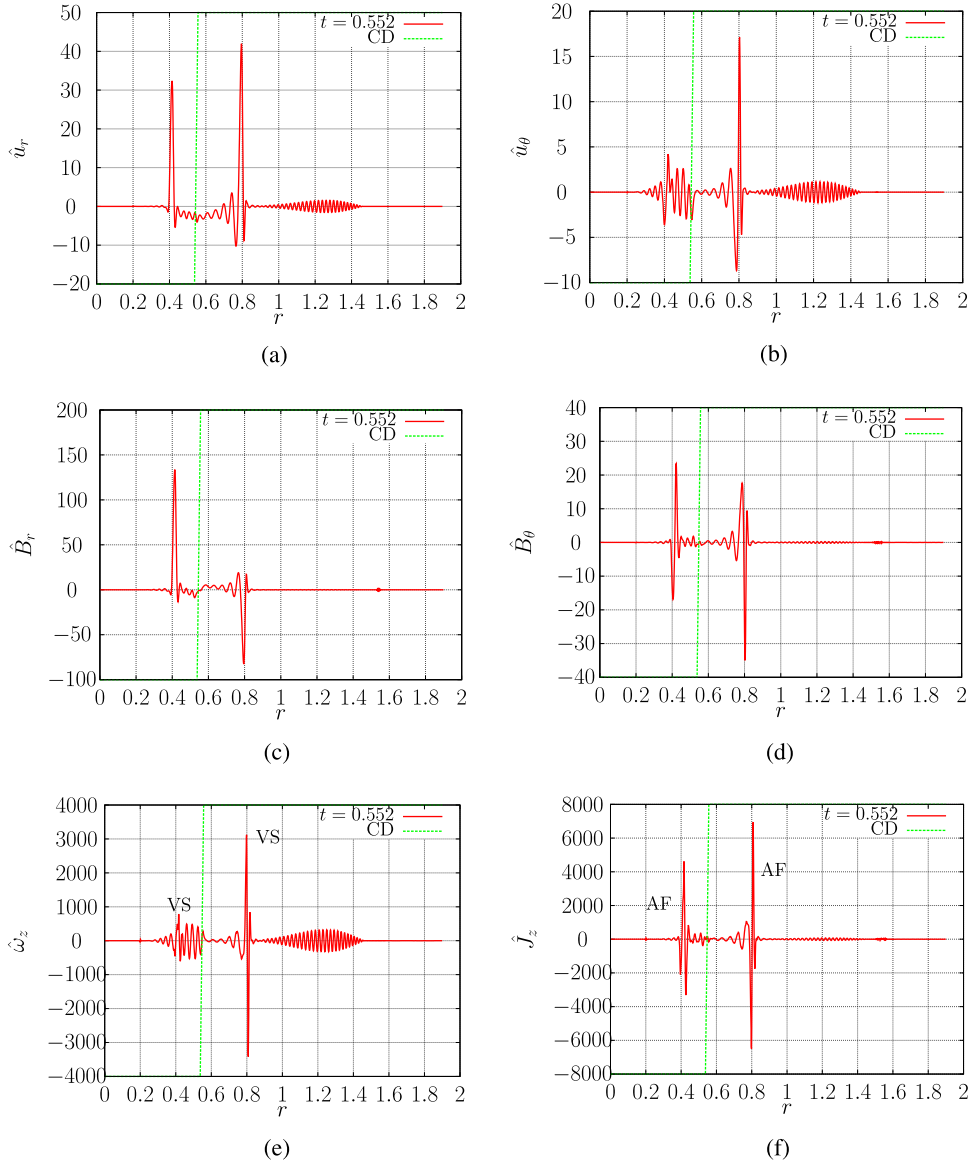
FIG. 12. Profiles of perturbed variables in MHD: (a) r-component of velocity, (b) θ-component of velocity, (c) r-component of magnetic field, (d) θ-component of magnetic field, (e) z-component of vorticity, (f) z-component of current density. The perturbation wavenumber is $m = 256$ and the initial plasma beta is $\beta = 4$ at the interface $R_0 = 1.0$.

oscillates around a small value below zero. The behavior is very similar to that observed for the azimuthal perturbations. For the smaller wavenumber cases ($k = 64, 16$), the time duration of the simulation is insufficient for significant suppression to occur. In all these cases, the onset of RTI is not clearly demarcated from the RMI phase.

We now examine the solution for $k = 256$ for which the suppression of the instability is the largest. The θ-component of vorticity and θ-component of current density $\hat{j}_\theta = ik\hat{B}_r - \frac{\partial(r\hat{B}_z)}{\partial r}$ are plotted in Fig. 14. The two vortex sheets evident in the vorticity plot are coincident with the Alfvén fronts seen in current density. The interface, devoid of the large initial baroclinic vorticity, loses the main driving mechanism of the instability and perturbation growth is significantly suppressed.

c. Combined azimuthal-axial perturbations. The time histories of normalized growth rate in the MHD case for different combinations of axial/azimuthal wavenumbers $(k, m) = (16, 16), (16, 64),$ $(16, 128), (16, 256), (64, 16), (128, 16), (256, 16), (256, 256)$ are plotted in Fig. 15. For these cases, we
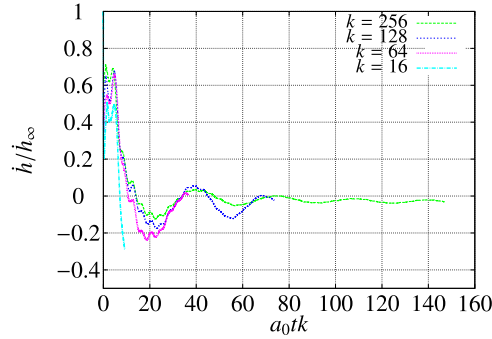
FIG. 13. Time history of scaled growth rate in MHD for axial perturbation wavenumber $k = 16, 64, 128, 256$. The initial plasma beta is $\beta = 4$ at the interface $R_0 = 1.0$.

chose the plasma beta to be $\beta = 2$ at the interface $R_0 = 1.0$. While the instability is suppressed for these wavenumber combinations, the suppression is still somewhat less than that observed for $\beta = 4$ for purely axial or azimuthal perturbations. Another noteworthy feature can be distinguished by comparing the $(k, m) = (16, 128), (128, 16)$ combinations. Both show similar overall behavior, but the oscillations associated with transverse reverberations in the higher azimuthal wavenumber persist while those in the higher axial wavenumber are nearly absent.

d. Vorticity spacetime evolution. To further elaborate on the vorticity evolution and distinguish between the MHD and hydrodynamics cases, we plot the vorticity space-time diagram for perturbation wavenumber $m = 256$ in Fig. 16. In hydrodynamics, the vorticity is confined to the interface and undergoes a sign change in keeping with the phase change associated with the RTI phase. Moreover, the vorticity on the interface increases in magnitude as time progresses. In MHD, on the other hand, the dominant vorticity is on Alfvén waves which straddle the interface in the spacetime diagram. There is also some evidence of weak secondary vorticity in the spacetime diagram but this is of little consequence for the growth of the instability.

C. Effect of converging geometry

Here we exclusively focus on the effect of converging geometry on high wave number perturbations. It is evident that for large radius, high wave number perturbations should effectively behave similarly to those in Cartesian geometry. Furthermore, as the mean interface translates radially inwards, the effect of converging geometry on axial and azimuthal wave number perturbations is expected to be different because in the axial case the wavelength of perturbation remains the same, whereas the wavelength decreases for the azimuthal case. We plot the normalized growth rate (scaled by their appropriate value of $\dot{h}_\infty$) for 2D perturbations in the planar and cylindrical
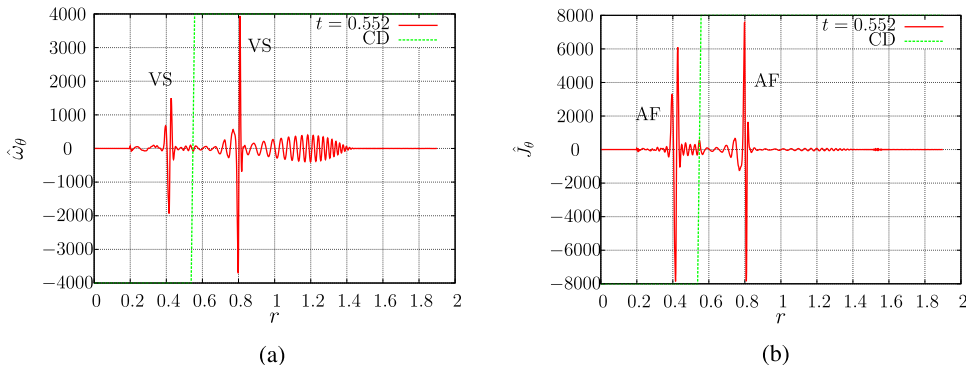

FIG. 14. Profiles of perturbed variables in MHD: (a) θ-component of vorticity, (b) θ-component of current density. The perturbation wavenumber is $k = 256$ and the initial plasma beta is $\beta = 4$ at the interface $R_0 = 1.0$.
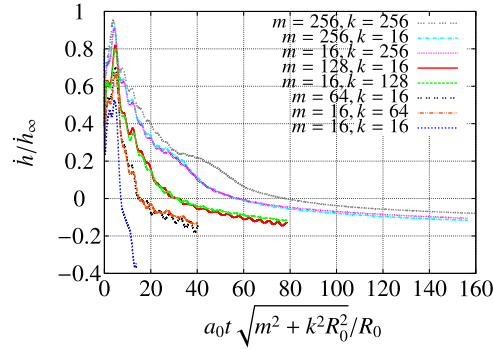
FIG. 15. Time history of scaled growth rate for 3D perturbations MHD for different wave number combinations for $\beta = 2$.

cases, for hydrodynamics in Figure 17(a), and for MHD in Figure 17(b). The wavenumber for 2-D perturbations in planar geometry is $k = 256$, and in cylindrical geometry for purely azimuthal (axial) modes is $m(k) = 256$. The effect of numerical diffusion is evident upon scrutiny in the planar case: this is manifested as a small decrease in the asymptotic growth rate. To mitigate the effects of numerical diffusion in this comparison, we choose a higher resolution of 6400 cells for the simulations discussed here. The planar case shows the characteristic growth rate development: early time oscillations until it settles down to a constant growth rate. The first peak in the growth rate is the same for planar and cylindrical cases (both axial and azimuthal). For scaled time beyond 40, the growth rate changes due to the effect of RTI in converging geometry. This effect is larger for the azimuthal case during the exponential increase in the RTI phase of the instability development. The MHD case investigated is for $\beta = 4$. Here we observe the same growth rate pattern in both planar and cylindrical cases for scaled time up to 20. The planar case growth rate oscillates about an asymptotic value of zero indicating almost complete suppression of the instability. In cylindrical geometry, the growth rate for both axial and azimuthal perturbations is nearly the same until scaled time of about 40. We observe a decrease in the period for the azimuthal case. In the cylindrical case, the oscillations occur about a mean value smaller than zero indicating a residual growth due to incomplete suppression during the RTI phase.

An important measure is the ratio of amplitude to wavelength of the perturbation to estimate the time duration during which the linear stability analysis is valid. Generally, conventional wisdom suggests that as long as the perturbation amplitude to wavelength is smaller than 0.1 linear analysis is a valid approximation. However, one notes that in linear analysis, the initial amplitude of the perturbation gets scaled out. We can, nonetheless, estimate the factor by which an initial perturbation amplitude will change. Defining the factor $\chi(t) = \frac{h(t)}{\lambda(t)} / \frac{h(0)}{\lambda(0)}$, where $h(t)$ is the perturbation amplitude and $\lambda(t)$ is the perturbation wavelength at time t. This definition accounts for the fact that the perturbation wavelength changes for azimuthal perturbations. This amplification measure can be estimated by the growth rate of the perturbations at the interface. For hydrodynamics: in the
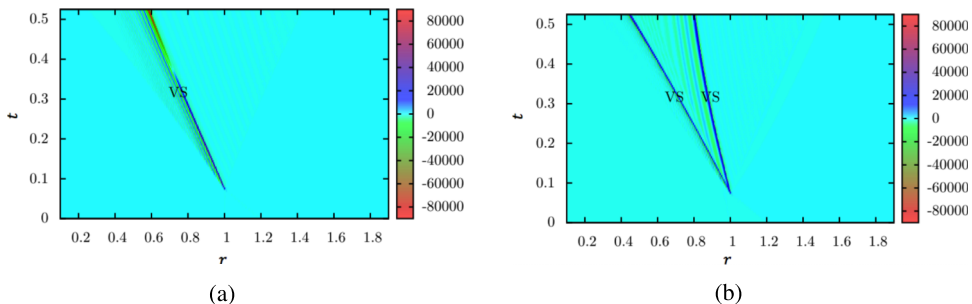

FIG. 16. (a) Spacetime diagram of vorticity $\hat{\omega}_z$ for hydrodynamics. (b) Spacetime diagram of vorticity $\hat{\omega}_z$ for MHD. The perturbation wavenumber is $m = 256$ and the plasma beta is $\beta = 4$ for MHD.
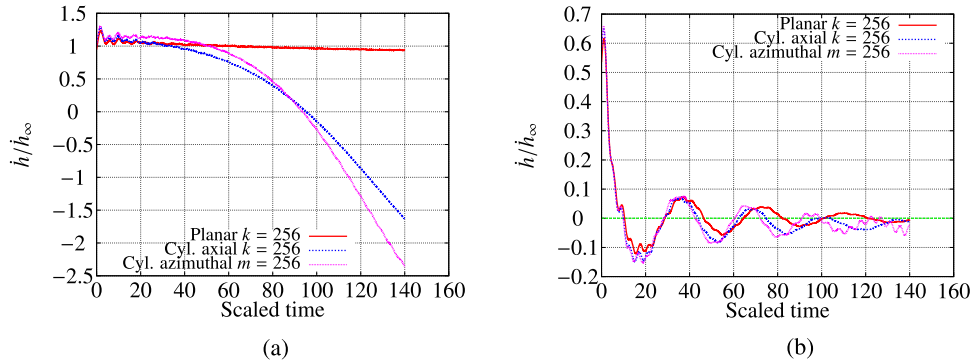
FIG. 17. Time history of scaled growth rate of planar and cylindrical geometries for $k = 256$ and $m = 256$. (a) Hydrodynamics case and (b) MHD case for $\beta = 4$.

planar case $\chi(t)$ is estimated to be $\chi(0.5) \approx 48$; for axial perturbations, the peak in χ is attained at $t \approx 0.26$ and is $\chi(0.26) \approx 22$, and $\chi(0.5) \approx -10$; whereas for azimuthal perturbations, peak value is $\chi(0.28) \approx 31$ and $\chi(0.5) \approx -32$. For the MHD simulations: in the planar case $\chi(t)$ is estimated to be $\chi(0.5) \approx 2.4$; for axial perturbations, the peak magnitude is $\chi(0.5) \approx 1.5$; for azimuthal perturbations, peak magnitude is $\chi(0.5) \approx 2.5$. Using these amplification estimates of the perturbation amplitude, and given the initial amplitude magnitude, one can estimate the time duration of validity of the linear simulations. In the hydrodynamics case, if the initial amplitude to wavelength ratio is smaller than 2×10^{-3} (planar case), 4.5×10^{-3} (axial perturbations), and 3.7×10^{-3} (azimuthal perturbations), the final amplitude to wavelength ratio will be smaller than 0.1, and hence linear stability results will be approximately valid during the entire time duration of the simulation. In the MHD case, we estimate that if the initial amplitude to wavelength ratios is smaller than 4×10^{-2} (planar case), 6.7×10^{-2} (axial perturbations) and 4×10^{-2} (azimuthal perturbations), the final amplitude to wavelength ratio will be smaller than 0.1, and conclude that linear stability results will be approximately valid during the entire time duration of the simulation. Moreover, for the converging MHD cases the amplitude actually reduces during the RTI phase but never exceeds in magnitude the asymptotic value attained in the planar case.

D. Effect of magnetic field strength

We now examine the effect of initial magnetic field strength characterized by the non-dimensional parameter β. The time history of scaled growth rate in MHD for plasma beta $\beta = \infty(\text{HD}), 256, 64, 4, 2$ is shown in Fig. 18, 2-D perturbations of azimuthal wavenumber $m = 256$, Fig. 18(a), and axial wavenumber $k = 256$, Fig. 18(b). The 3D perturbations case we chose were $\beta = \infty(\text{HD}), 16, 4, 2, 1$ and the perturbation wavenumbers are $k = m = 256$, Fig. 18(c). As expected the smallest $\beta \leq 4$, (largest magnetic field) has the strongest suppression of the instability for both the azimuthal and axial perturbation cases. Interestingly, the weakest magnetic field case ($\beta = 256$) halts the exponential increase in the magnitude of the growth rate during the RTI phase. We observe a second frequency related to the speed of the Alfvén fronts. The Alfvén speed is proportional to $\beta^{-\frac{1}{2}}$. Comparing the time histories in Figure 18 for $\beta = 256$ to $\beta = 64$, we observe the first local minimum shift from $t \approx 128$ to $t \approx 64$ representing a period halving, and comparing $\beta = 64$ to $\beta = 4$ we observe roughly a decrease by a factor of four in the period of the oscillations. We further point out that even though growth rates for the azimuthal and axial cases seem remarkably similar, there are subtle differences.

E. Comparison between linear and nonlinear simulations

Nonlinear simulations for RMI are performed using the ideal MHD equations expressed in strong conservation form. The numerical method is a predictor-corrector unsplit method in cylindrical coordinates, and is similar to that developed by Samtaney[9] and Samtaney *et al.*[23] A seven-wave linearized Riemann solver method is used to compute the fluxes; and the solenoidal condition on the magnetic
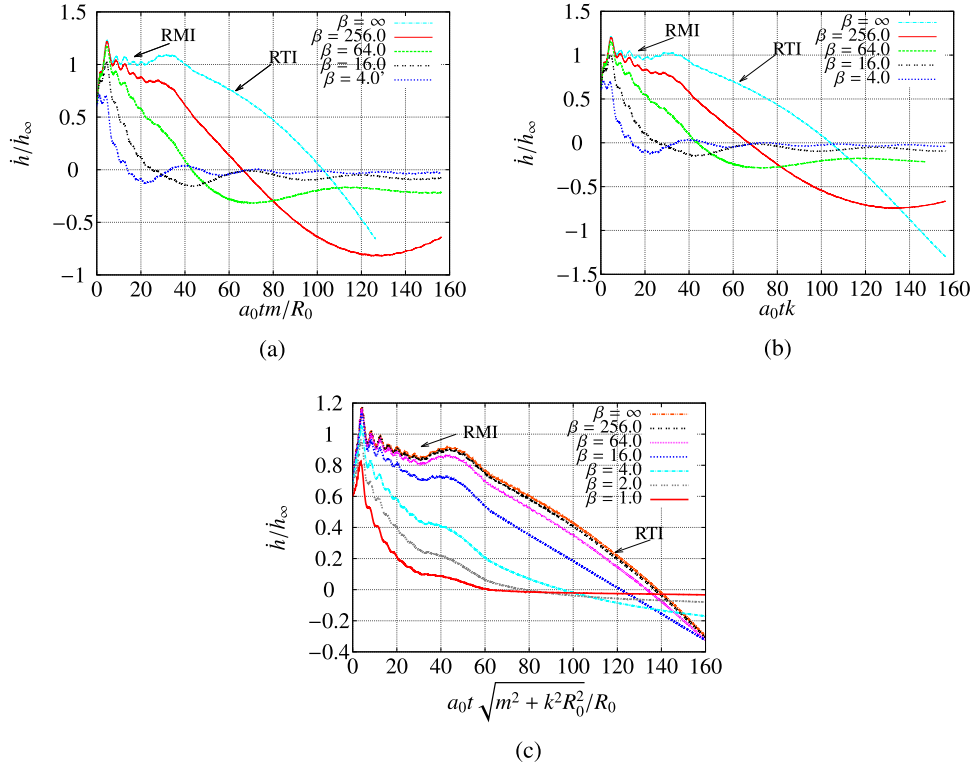
FIG. 18. Time history of scaled growth rate in MHD for plasma beta $\beta = \infty (HD), 256, 64, 4, 2$ at the interface for (a) $m = 256$, $k = 0$, (b) $m = 0$, $k = 256$, and (c) $\beta = \infty (HD), 16, 4, 2, 1$ for $m = 256$, $k = 256$. (a) Purely azimuthal perturbations $m = 256$. (b) Purely axial perturbations $k = 256$. (c) 3D perturbations $m = 256, k = 256$.

field is maintained by a projection technique. The nonlinear simulation is conducted on a grid extending azimuthally from $\theta = 0$ to $2\pi/128$ with periodic boundary conditions applied at these bounds. In the radial direction, the grid extended from $r = 0.3$ to 1.9. The boundary conditions applied at these bounds are identical to those applied in the linearized simulations. The Chisnell-type shock is initialized at $R_s = 1.2$ and the initial interface location is $R_0 = 1$, as for the linearized simulations. The computational grid has 3000 (8000) cells in the radial direction for $m = 16$ ($m = 128$) and 128 cells in the azimuthal direction. Examining a snapshot of density and vorticity for wavenumber $m = 16$ and magnetic field $\beta = 4$ in the nonlinear simulation, shown in Fig. 19(a), shows clear evidence of vorticity on MHD shock fronts and none on the interface. These observations are similar to those in Wheatley *et al.*[11] for the Cartesian case. For this case, a comparison of the perturbation growth rate between linear and nonlinear simulations is shown in Fig. 19(b). Further comparisons of the nonlinear growth rate of a single mode interface in the linear and nonlinear simulations are shown for wavenumber $m = 16$ and a lower value of the magnetic field $\beta = 16$ in Fig. 19(c), and for a higher wavenumber $m = 128$ in Fig. 19(d). The linear simulations performed here had the same number of radial cells as the nonlinear simulations. In Fig. 19(d), we also plot the growth rate for linear simulations using 1600 cells. The difference in linear simulations at 1600 and 8000 cells is relatively small and one may consider this as a rudimentary convergence test (further discussion on convergence is in the Appendix).

The initial amplitude of the interface in the nonlinear simulation is chosen to be 5% of the wavelength, i.e., $\frac{1}{20}\frac{2\pi}{m}$. In the nonlinear case, the perturbation amplitude is compressed by the incident shock. In linear theory, the amplitude of perturbation is arbitrary and the compression by the incident shock is not part of the linear theory. The growth rate comparison is performed after the incident shock passage over the perturbed interface. The nonlinear and linear growth rates show satisfactory agreement at early times. As nonlinear effects become important, the agreement worsens at late times for the low wavenumber cases ($m = 16$) particularly for the weaker magnetic field case ($\beta = 16$).
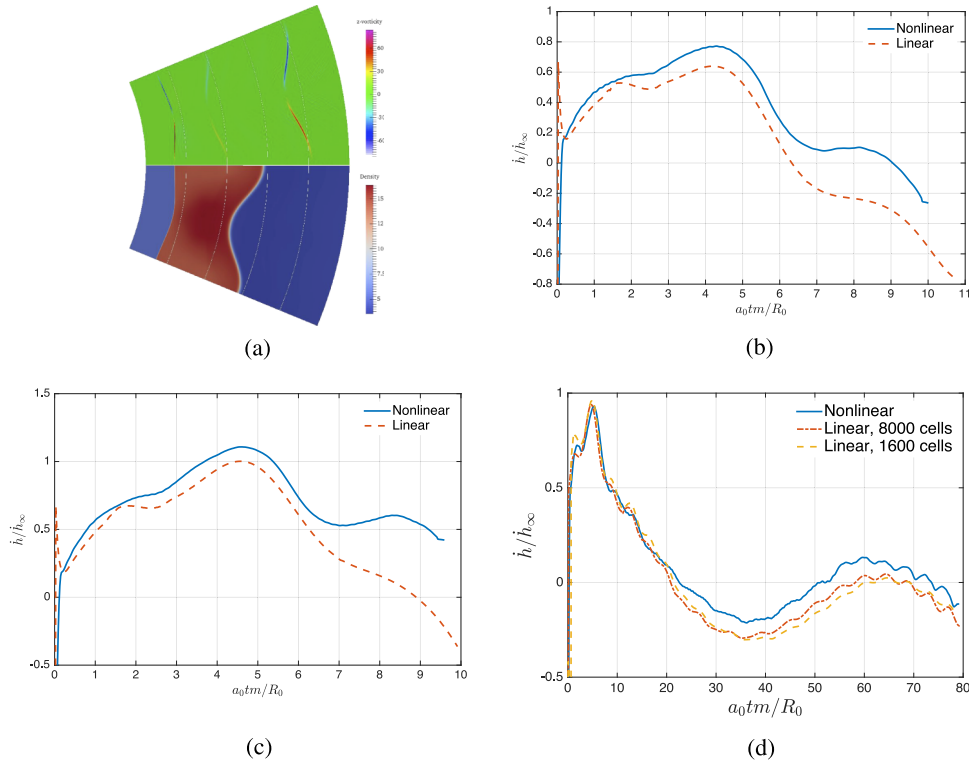
FIG. 19. (a) Density and vorticity snapshot in nonlinear simulation. (b)-(d) Comparison of nonlinear growth rate between linear and nonlinear simulations. (a) Nonlinear simulation, $m = 16, \beta = 4$. (b) $m = 16, \beta = 4$. (c) $m = 16, \beta = 16$. (d) $m = 128, \beta = 16$.

IV. CONCLUSION

In this paper, linearized ideal MHD equations with a time-dependent base state with discontinuities have been solved numerically. The numerical linear stability analysis is performed in cylindrical geometry, with purely azimuthal or axial perturbations at a positive Atwood number interface that interacts with a Chisnell-type imploding shock. In hydrodynamics, the Richtmyer-Meshkov instability is driven by the baroclinic vorticity deposited by the incident shock on the interface, followed by Rayleigh-Taylor instability which dominates the growth rate. The transition from RMI to RTI in cylindrical geometry is accompanied by a phase change in the perturbation amplitude. Moreover, this transition between RMI and RTI is most evident for the highest wavenumbers investigated, and not so clearly demarcated for low wavenumbers. The growth rate during the RMI phase is proportional to the wavenumber (m or k) and agrees well, for large wave numbers, with the asymptotic growth rate $\dot{h}_\infty$ of Lombardini and Pullin. For the MHD cases, the suppression of the instability is most evident for large wavenumbers and magnetic field strengths characterized by $\beta = 4$ or less are sufficient to suppress the growth rate at the interface. There is a residual small growth rate associated with the RTI. The mechanism of suppression is the transport of vorticity away from the density interface by two Alfvén fronts.

The present research can be further extended in many aspects, such as linear stability in spherical geometry, simulating flows with multiple interfaces, applying other magnetic field configurations, and including negative Atwood ratio interfaces.

ACKNOWLEDGMENTS

APPENDIX: NUMERICAL METHOD

In this section, we describe the numerical method that solves the ideal MHD Eq. (9), following the method originally developed by Samtaney.[18]

We use the method-of-lines approach for the time discretization by rewriting Eq. (9a) as $\frac{\partial \mathring{U}}{\partial t} = R(\mathring{U})$, and adopting the third order TVD Runge-kutta time discretization approach as

$$
\begin{aligned}
\mathring{U}_0 &= \mathring{U}^n, \\
\mathring{U}_1 &= \mathring{U}_0 + \Delta t R(\mathring{U}_0), \\
\mathring{U}_2 &= \frac{3}{4}\mathring{U}_0 + \frac{1}{4}\mathring{U}_1 + \frac{\Delta t}{4}R(\mathring{U}_1), \\
\mathring{U}_3 &= \frac{1}{3}\mathring{U}_0 + \frac{2}{3}\mathring{U}_2 + \frac{2\Delta t}{3}R(\mathring{U}_2), \\
\mathring{U}^{n+1} &= \mathring{U}_3,
\end{aligned}
\tag{A1}
$$

where Δt is the time step and $\mathring{U}^n$ is the solution at time step n. The perturbed state equation (9b) is similarly updated.

A finite volume method is adopted for the spatial discretization in which we define the solution vectors at the centroids of the subintervals indexed as j. The fluxes are computed at the faces indexed as $j \pm \frac{1}{2}$ and then used to update the solution at the centroids.

The Jacobian matrix $M(\mathring{U})$ is singular and hence we adopt the seven wave method to compute the fluxes.[23] Denoting the remaining seven variables and their fluxes by an over-bar, we express the flux of the base state and perturbed quantities as

$$
\bar{F}(\mathring{U})\big|_{j+\frac{1}{2}} = \frac{1}{2}(\bar{F}(\bar{\mathring{U}}_{L,j+\frac{1}{2}}, \mathring{B}_r) - \bar{F}(\bar{\mathring{U}}_{R,j+\frac{1}{2}}, \mathring{B}_r)) - \frac{1}{2}\sum_{k=1}^{7}\alpha_k \mathbf{r}_k,
\tag{A2}
$$

$$
[\bar{M}(\mathring{U})\bar{U}]\big|_{j+\frac{1}{2}} = \frac{1}{2}(\bar{M}_{j+\frac{1}{2}}\bar{U}_{L,j+\frac{1}{2}} + \bar{M}_{j+\frac{1}{2}}\bar{U}_{R,j+\frac{1}{2}}) - \frac{1}{2}|\bar{M}|_{j+\frac{1}{2}}(\bar{U}_{R,j+\frac{1}{2}} - \bar{U}_{L,j+\frac{1}{2}}),
\tag{A3}
$$

where $|\bar{M}| = \bar{M}^+ - \bar{M}^-$, $\mathbf{l}_k$ and $\mathbf{r}_k$ are the left and right eigenvectors of $\bar{M}$ ($\bar{M}$ is M after deleting the row/column corresponding to $\mathring{B}_r$), $\alpha_k = \mathbf{l}_k \cdot (\bar{\mathring{U}}_{R,j+\frac{1}{2}} - \bar{\mathring{U}}_{L,j+\frac{1}{2}})$. At each side of interface $j + \frac{1}{2}$, both the base state and the perturbed quantities ($\bar{\mathring{U}}_{L/R,j+\frac{1}{2}}$ and $\bar{\hat{U}}_{L/R,j+\frac{1}{2}}$) are obtained by fitting linear profiles and slope limiting. In the seven-wave method, the contribution $\hat{B}_r$ with other variables is considered by including the following term to the RHS of Eq. (9b):

$$
C(\mathring{U}, \hat{B}_r) = [0, \gamma\mathring{B}_r^1 + B_r^*, \mathring{B}_\theta, \mathring{B}_z, \mathring{u}_\theta, \mathring{u}_z, (\gamma\mathring{B}_r^1\mathring{u}_r + \mathring{B}_\theta\mathring{u}_\theta + \mathring{B}_z\mathring{u}_z)]^T \frac{1}{r}\frac{\partial(r\hat{B}_r^1)}{\partial r}.
\tag{A4}
$$

At the final stage of each time step, maintaining the solenoidal property of the magnetic field requires updating the perturbed variables $\hat{B}_\theta$ and $\hat{B}_z$ as follows:

- For purely azimuthal perturbation:

$$
\hat{B}_\theta\big|_j = \frac{i}{m}\frac{\partial}{\partial r}(r\hat{B}_r^1)\bigg|_j \approx \frac{i}{m}\frac{r\hat{B}_r^1\big|_{j+1} - r\hat{B}_r^1\big|_{j-1}}{2\Delta r}.
\tag{A5}
$$

- For purely axial perturbations:

$$
\hat{B}_z\big|_j = \frac{i}{kr_j}\frac{\partial}{\partial r}(r\hat{B}_r^1)\bigg|_j \approx \frac{i}{kr_j}\frac{r\hat{B}_r^1\big|_{j+1} - r\hat{B}_r^1\big|_{j-1}}{2\Delta r}.
\tag{A6}
$$

All of $\hat{B}_r^1$, $\hat{B}_\theta$, and $\hat{B}_z$ in Eqs. (A5) and (A6) are at the same time step.

In combined axial/azimuthal perturbation simulations, numerical solutions may not satisfy $\nabla \cdot B = 0$ because of discretization errors. We employ a projection technique outlined below to ensure the solenoidal property of the magnetic field. The projection method requires the solution of

the following Poisson equation:

$$\nabla^2 \zeta = \nabla \cdot B,$$
$$\zeta|_{R_l} = \zeta|_{R_r} = 0. \tag{A7}$$

For finite volume approximation, the discretization of Equation (A7) is written as

$$\frac{1}{r_j} \frac{(r\zeta)|_{j+\frac{1}{2}} + (r\zeta)|_{j-\frac{1}{2}} - (r_{j+\frac{1}{2}} + r_{j-\frac{1}{2}})\zeta_j}{(\Delta r)^2} - (\frac{m^2}{r_j^2} + k^2)\zeta_j$$
$$= \frac{1}{r_j} \frac{(rB_r^1)|_{j+\frac{1}{2}} - (rB_r^1)|_{j-\frac{1}{2}}}{\Delta r} + i(\frac{m}{r_j}B_{\theta,j} + kB_{z,j}), \tag{A8}$$

$$r_j((r\zeta)|_{j+\frac{1}{2}} + (r\zeta)|_{j-\frac{1}{2}} - (r_{j+\frac{1}{2}} + r_{j-\frac{1}{2}})\zeta_j) - (\Delta r)^2(m^2 + r_j^2 k^2)\zeta_j$$
$$= r_j \Delta r((rB_r^1)|_{j+\frac{1}{2}} - (rB_r^1)|_{j-\frac{1}{2}}) + (\Delta r)^2 i(mr_j B_{\theta,j} + kr_j^2 B_{z,j}). \tag{A9}$$

The above tridiagonal system is solved using the standard Thomas algorithm. The corrected magnetic field is $B^c = B - \nabla\zeta$ and is divergence free. Each component is updated as follows:

$$B_r^c|_{j\pm\frac{1}{2}} = B_r^1|_{j\pm\frac{1}{2}} - \frac{\partial \zeta}{\partial r}|_{j\pm\frac{1}{2}},$$
$$B_\theta^c|_j = B_\theta|_j - \frac{im}{r_j}\zeta|_j,$$
$$B_z^c|_j = B_z|_j - ik\zeta|_j. \tag{A10}$$

Numerical convergence. In this paper, we have not presented detailed results on numerical convergence and order of accuracy of the proposed method. Numerical convergence tests of this method, performed by Gao,[24] show second order accuracy for smooth initial conditions. The method proposed here is very similar to that developed by Samtaney[18] for Cartesian slab geometry, which exhibits second order convergence for smooth flows and convergence rates between one and two for flows with shocks. In Section III E, linear simulations for $m = 128, \beta = 16$ (Fig. 19) show a small difference in the growth rate at two mesh resolutions of 1600 and 8000 radial cells. Other such convergence tests were also performed for other parameters and showed little difference in the growth rate at mesh resolutions of 1600 and 3200 radial cells.

[1] R. D. Richtmyer, "Taylor instability in shock acceleration of compressible fluids," Commun. Pure Appl. Math. **13**(2), 297–319 (1960).

[2] E. E. Meshkov, "Instability of the interface of two gases accelerated by a shock wave," Fluid Dynamics **4**(5), 101–104 (1969).

[3] M. Brouillette, "The Richtmyer-Meshkov instability," Ann. Rev. Fluid Mech. **34**, 445–468 (2002).

[4] J. D. Lindl, R. L. McCrory, and E. M. Campbell, "Progress toward ignition and burn propagation in inertial confinement fusion," Phys. Today **45**(9), 32–40 (1992).

[5] J. Lindl, O. Landen, J. Edwards, E. Moses, NIC Team *et al.*, "Review of the national ignition campaign 2009-2012," Phys. Plasmas **21**(2), 020501 (2014).

[6] D. Arnett, "The role of mixing in astrophysics," Astrophys. J., Suppl. Ser. **127**(2), 213–217 (2000).

[7] J. Yang, T. Kubota, and E. E. Zukoski, "Applications of shock-induced mixing to supersonic combustion," AIAA J. **31**(5), 854–862 (1993).

[8] A. M. Khokhlov, E. S. Oran, and G. O. Thomas, "Numerical simulation of deflagration-to-detonation transition: The role of shock–flame interactions in turbulent flames," Combust. Flame **117**(1), 323–339 (1999).

[9] R. Samtaney, "Suppression of the Richtmyer-Meshkov instability in the presence of a magnetic field," Phys. Fluids **15**(8), L53–L56 (2003).

[10] V. Wheatley, D. I. Pullin, and R. Samtaney, "Stability of an impulsively accelerated density interface in magnetohydrodynamics," Phys. Rev. Lett. **95**, 125002 (2005).

[11] V. Wheatley, R. Samtaney, and D. I. Pullin, "The Richtmyer-Meshkov instability in magnetohydrodynamics," Phys. Fluids **21**(8), 082102 (2009).

[12] V. Wheatley, R. Samtaney, D. I. Pullin, and R. M. Gehre, "The transverse field Richtmyer-Meshkov instability in magnetohydrodynamics," Phys. Fluids **26**(1), 016102 (2014).

[13] Q. Zhang and M. J. Graham, "A numerical study of Richtmyer–Meshkov instability driven by cylindrical shocks," Phys. Fluids **10**(4), 974–992 (1998).

[14] M. Lombardini and D. I. Pullin, "Small-amplitude perturbations in the three-dimensional cylindrical Richtmyer-Meshkov instability," Phys. Fluids **21**(11), 114103 (2009).

[15] K. O. Mikaelian, "Rayleigh-Taylor and Richtmyer-Meshkov instabilities and mixing in stratified spherical shells," Phys. Rev. A **42**(6), 3400 (1990).

[16] K. O. Mikaelian, "Rayleigh-Taylor and Richtmyer-Meshkov instabilities and mixing in stratified cylindrical shells," Phys. Fluids **17**(9), 094105 (2005).

[17] Y. Yang, Q. Zhang, and D. H. Sharp, "Small amplitude theory of Richtmyer–Meshkov instability," Phys. Fluids **6**(5), 1856–1873 (1994).

[18] R. Samtaney, "A method to simulate linear stability of impulsively accelerated density interfaces in ideal-MHD and gas dynamics," J. Comput. Phys. **228**(18), 6773–6783 (2009).

[19] R. F. Chisnell, "An analytic description of converging shock waves," J. Fluid Mech. **354**, 357–375 (1998).

[20] W. Mostert, V. Wheatley, R. Samtaney, and D. I. Pullin, "Effects of seed magnetic fields on magnetohydrodynamic implosion structure and dynamics," Phys. Fluids **26**(12), 126102 (2014).

[21] J. F. Hawley and N. J. Zabusky, "Vortex paradigm for shock-accelerated density-stratified interfaces," Phys. Rev. Lett. **63**, 1241–1244 (1989).

[22] R. Samtaney and N. J. Zabusky, "Circulation deposition on shock-accelerated planar and curved density-stratified interfaces: Models and scaling laws," J. Fluid Mech. **269**, 45–78 (1994).

[23] R. Samtaney, P. Colella, T. J. Ligocki, D. F. Martin, and S. C. Jardin, "An adaptive mesh semi-implicit conservative unsplit method for resistive MHD," J. Phys.: Conf. Ser. **16**(1), 40 (2005).

[24] S. Gao, "Linear simulations of the cylindrical Richtmyer-Meshkov instability in hydrodynamics and MHD," MS thesis, King Abdullah University of Science and Technology, 2013.